

Abstract

This is the first paper to investigate the relationship between the scattering phase function of cirrus and the relative humidity with respect to ice (RH_i), using space-based solar radiometric angle-dependent measurements. The relationship between RH_i and the complexity of ice crystals has been previously studied using data from aircraft field campaigns and laboratory cloud chambers. However, to the best of our knowledge, there have been no studies to date that explore this relationship, through the use of remotely sensed space-based angle-dependent solar radiometric measurements. In this paper, a case study of semi-transparent cirrus is used to explore the possibility of such a relationship. Moreover, for the first time, RH_i fields predicted by a high-resolution numerical weather prediction (NWP) model are combined with satellite retrievals of ice crystal complexity. The NWP model was initialised at midnight, on the 25 January 2010, and the mid-latitude RH_i field was extracted from the NWP model at 13:00 UTC. At about the same time, there was a Polarization and Anisotropy of Reflectance for Atmospheric science coupled with Observations from a Lidar (PARASOL) overpass, and the PARASOL swath covered the NWP model predicted RH_i field. The cirrus case was located over Scotland, and over the North Sea. From the satellite channel based at $0.865 \mu\text{m}$, the directionally averaged and directional spherical albedos were retrieved between the scattering angles of about 80° and 130° . An ensemble model of cirrus ice crystals is used to predict phase functions that vary between phase functions that exhibit optical features (called pristine), to featureless phase functions. For each of the PARASOL pixels, the phase function that best minimised differences between the spherical albedos was selected. This paper reports a positive correlation between the scattering phase function and RH_i . That is, the pristine and completely featureless phase functions are found to be correlated with $RH_i < 100\%$, and $RH_i > 100\%$, respectively. Moreover, it is demonstrated that the NWP model prediction of the vertical profile of RH_i is in good agreement with independent aircraft-based physical retrievals of RH_i .

Scattering phase function of cirrus and the atmospheric state

A. J. Baran et al.

Title Page

Abstract

Introduction

Conclusions

References

Tables

Figures



Back

Close

Full Screen / Esc

Printer-friendly Version

Interactive Discussion



Furthermore, the NWP model prediction of the cirrus cloud-top height and its vertical extent is also found to be in good agreement with aircraft-based lidar measurements.

1 Introduction

Cirrus or pure ice crystal cloud usually forms at temperatures of less than about -40°C , and at altitudes greater than about 6 km (Wylie et al., 1999; Baran, 2012; Guignard et al., 2012). The extent to which ice crystals can grow and form complex shapes is dependent on the environmental temperature, pressure, and RH_i (Marshall and Langleben 1954; Nakaya 1954; Hallett and Mason 1958; Mason 1971; Heymsfield 1977; Liou 1986; Lynch 2002; Bailey and Hallett 2004; Bailey and Hallett 2009; Pfalzgraff et al., 2010; Ulanowski et al., 2013). In cirrus clouds, the supersaturations with respect to ice can range between about 150 % to -50 % (Krämer et al., 2009). However, more recent studies of RH_i in mid-latitude cirrus, report values of about 60 % to 120 % (Gayet et al., 2011; Ulanowski et al., 2013), with the latter values being the more typical. With such a range of possible supersaturation values reported by previous authors, the range of ice crystal complexity, within the same cirrus cloud, is likely to be significant (Bailey and Hallett, 2009). In this paper, ice crystal complexity can mean polycrystals, which may be compact or highly irregular, and ice aggregates, and these ice aggregates may also have low aspect ratios (i.e., the ratio between the projected area of the non-spherical particle and the projected area of the circumscribing circle of the same maximum dimension as the non-spherical particle). The monomers that make-up the polycrystal or aggregate may also be surface roughened on their facets and/or contain air cavities, within their volumes.

The role of ice supersaturation in forming complex ice crystals has most recently been studied by Bailey and Hallett (2009), Pfalzgraff et al. (2010) and Ulanowski et al. (2013). In the cloud chamber study by Pfalzgraff et al. (2010), it was reported that surface roughness was at its greatest when supersaturations were near zero. Moreover, Walden et al. (2003) observed surface roughness on precipitating ice crystals un-

Scattering phase function of cirrus and the atmospheric state

A. J. Baran et al.

Title Page

Abstract

Introduction

Conclusions

References

Tables

Figures



Back

Close

Full Screen / Esc

Printer-friendly Version

Interactive Discussion



**Scattering phase
function of cirrus and
the atmospheric state**

A. J. Baran et al.

Title Page

Abstract

Introduction

Conclusions

References

Tables

Figures



Back

Close

Full Screen / Esc

Printer-friendly Version

Interactive Discussion



der conditions of near-zero supersaturation at the South Pole. Other laboratory studies by (Bacon et al., 2003; Malkin et al., 2012; Ulanowski et al., 2013) show that ice crystals, under ice supersaturated conditions, can become surface roughened, through the development of prismatic grooves or dislocations on the ice crystal surface. However, as pointed out by Bacon et al. (2003) and others, the temperature and RH_i variables do not uniquely determine the number of monomers that make-up the polycrystal or surface roughness. This is because ice crystal complexity and surface roughness may also depend on how the ice crystals were initiated, and thus may depend on the chemical composition of the initiating ice nuclei. A recent paper by Ulanowski et al. (2013) reported that for a few cases of mid-latitude cirrus, formed in Oceanic air, slightly higher values of ice crystal complexity were found than was the case for mid-latitude cirrus formed in Continental air (i.e., a polluted air mass). However, in the same study, no correlation was found between ice crystal complexity and instantaneous measurements of RH_i . As pointed out by Ulanowski et al. (2013), this lack of correlation could be due to the instantaneous measurements being obtained at a single point in time, whereas the ice crystals, on which the measurements were based, may have gone through different histories of supersaturation, and so for each measurement, the history of supersaturation-exposure can never be known. On the other hand, controlled laboratory studies by Ulanowski et al. (2013) of ice crystal analogues, show that under high levels of ice supersaturation, the ice crystals formed can be very complex relative to the regular ice crystals grown under conditions of low ice supersaturation. This latter laboratory study of Ulanowski et al. (2013) is consistent with the findings of Bailey and Hallett (2009).

Theoretical light scattering studies by (Schmitt and Heymsfield 2010; Macke et al., 1996a, b; Yang and Liou 1998; Yang et al., 2008) have shown that the processes of surface roughness and air inclusions within ice crystals can profoundly alter their scattering phase functions. As surface roughness increases, the 22° and 46° halos are reduced or completely removed, resulting in featureless phase functions with a high degree of side scattering. This high degree of side scattering results in surface rough-

**Scattering phase
function of cirrus and
the atmospheric state**

A. J. Baran et al.

Title Page

Abstract

Introduction

Conclusions

References

Tables

Figures



Back

Close

Full Screen / Esc

Printer-friendly Version

Interactive Discussion



Polar Nephelometer (PN), which is described by Gayet et al. (1997), have been used to measure the angular scattered intensity of naturally-occurring single ice crystals, at scattering angles between about 15° and 162° , at the wavelength of $0.80\ \mu\text{m}$. Clearly, the PN measured polar angle range encompasses the halo regions of 22° and 46° .

Therefore, obtaining the ratio of the ice crystal scattered energy at the polar angle of 22° to that at 18.5° (the latter being an angle at which no halo is formed by prismatic ice crystals) would be a quantitative measure of the presence of the 22° halo. Halo ratios greater than one are likely to be associated with pristine ice crystals, whilst halo ratios less than one are likely to be associated with irregular ice crystals. Using a mid-latitude cirrus case, Gayet et al. (2011) used the halo ratio to relate the occurrence of halos to instantaneous measurements of RH_i . The study found that at the trailing edge of the cirrus-band, at a temperature of -55°C , the halo ratio < 1 , but at the leading edge of the cirrus-band, the halo ratio > 1 , at a temperature of -27°C . The study did not find any systematic evidence for a relationship between the halo ratio and ice supersaturation, a finding that is consistent with Ulanowski et al. (2013). However, Gayet et al. (2011) did find that halo ratios > 1 were more likely to be found at supersaturation values of around 100%, and no halo ratios > 1 were found at the highest supersaturation values, which approached 120%. Moreover, in the recent study by Ulanowski et al. (2013), a negative correlation is reported between the occurrence of halos and estimated ice crystal complexity. The measure of ice crystal complexity was derived from in situ observations of spatial light scattering patterns from single particles obtained in several cases of mid-latitude cirrus. The in situ findings of Gayet et al. (2011) and laboratory studies of Ulanowski et al. (2013) are consistent with previous studies (i.e., Bailey and Hallett, 2009, and references therein), which tend to show that more complex ice crystals are associated with relatively high values of RH_i .

The relationship between the scattering properties of atmospheric ice and the physical state in which the ice resides is important to explore, as this may lead to an improvement in the parameterization of ice optical properties in climate models. Such an improvement can only come about through a deeper understanding of how the growth

Scattering phase function of cirrus and the atmospheric state

A. J. Baran et al.

Title Page

Abstract

Introduction

Conclusions

References

Tables

Figures



Back

Close

Full Screen / Esc

Printer-friendly Version

Interactive Discussion



of ice crystal complexity is related to the atmospheric state. This relationship could then be used to predict appropriate ice scattering properties for some given atmospheric state, rather than assuming the same scattering properties for all states that are found in a climate model, which is what is done at the present time. The most recent report of the Intergovernmental Panel on Climate Change (IPCC, 2013) stated that the coupling between clouds and the atmosphere was one of the largest uncertainties in predicting climate change. This uncertainty may well be reduced if appropriate parameterizations could be found between ice crystal scattering properties and the atmospheric state.

In this paper, for a case of mid-latitude cirrus, the relationship between the scattering phase function and RH_i is further studied, by combining with space-based multi-angle total reflectance measurements an NWP prediction of the RH_i field. The paper is split into the following sections. Section 2 describes the NWP model, and the aircraft-based instruments used in this study. Section 3 describes the single-scattering properties of ice crystals on which the satellite retrievals are based, and a brief description of the radiative transfer model is also given. The retrieval methodology is described in Sect. 4 and results are discussed in Sect. 5. Section 6 presents the conclusions of this study.

2 The cirrus case, numerical weather prediction model and aircraft instrumentation

The cirrus case occurred on 25 January 2010 off the North and East coast of Scotland, and it is shown in Fig. 1. The figure shows a high-resolution MODerate Imaging Spectroradiometer (MODIS) composite image (Platnick et al., 2003) of semi-transparent cirrus obtained at 13:30 UTC. The semi-transparent cirrus can be clearly seen around the North and East Coast of Scotland, whilst further to the East, lower level water cloud underlying the cirrus can be seen. At about the same time, as the image shown in Fig. 1 was taken the FAAM (Facility for Airborne Atmospheric Measurements) BAe-146 aircraft was measuring the same high-cloud field.

**Scattering phase
function of cirrus and
the atmospheric state**

A. J. Baran et al.

Title Page

Abstract

Introduction

Conclusions

References

Tables

Figures



Back

Close

Full Screen / Esc

Printer-friendly Version

Interactive Discussion



The FAAM aircraft is an atmospheric research facility, which is jointly owned by the Met Office and the National Environment Research Council (NERC). The cirrus case shown in Fig. 1 was sampled by the aircraft as part of the ‘Constrain’ field programme (Cotton et al., 2013). The aircraft sampled the cirrus between the latitudes of about 58° N and 59° N, and between the longitudes of about 2.5° W and 4.5° W. The aircraft in situ instrumentation measured the temperatures of the cloud-top and base to be about -55°C and -30°C , respectively. The aircraft began sampling the cloud at 11:55:06 UTC, and finished the sampling at 15:49:44 UTC. During this sampling time, the aircraft flew three straight and level runs above the cloud, each of about 10 minutes duration, commencing at 13:19:00 UTC, 13:27:42 UTC, and at 15:21:42 UTC, respectively. From the aircraft a dropsonde (measures vertical profiles of temperature, pressure, and relative humidity with respect to water) was released at 13:30:00 UTC. In this study, use is made of the aircraft data from the earlier two runs, and the dropsonde measurements, which most closely coincided with the PARASOL overpass. Note also, that there was an 8 minute interval between the two earlier straight and level runs, during which time the aircraft was manoeuvring into position. In this paper, use is made of observations from two instruments deployed on the aircraft. The two instruments were the active Leosphere ALS450 elastic backscatter lidar and the passive Airborne Research Interferometer Evaluation System (ARIES).

The nadir-pointing lidar operates at 0.355 μm with an integration time of 2 s and a vertical resolution of 1.5 m (Marenco et al., 2011). Further averaging of the signals has been done at post-processing, bringing the temporal resolution to 10 s (equivalent at aircraft science speed to a 1.5–2 km footprint) and the vertical resolution to 45 m. The volume extinction coefficient is computed from the lidar returns using the Fernald-Klett method described in (Fernald 1984; Klett 1985), assuming a lidar ratio of 20 sr.

The ARIES instrument is fully described in Wilson et al. (1999), but briefly it is a modified Bomem MR200 interferometer, measuring infrared radiances between the wavelengths of 3.3 μm and 20.0 μm , at a spectral resolution of 1 cm^{-1} . The interferometer is capable of multiple viewing geometries both up and down, as well as cross-track.

The nadir-pointing ARIES and lidar data used here are from the straight and level runs above the cirrus.

The RH_i field of the cirrus case, shown in Fig. 1, has been simulated using the Met Office high-resolution numerical weather prediction model (NWP). The NWP simulation of the RH_i field was obtained using a high-resolution limited area model nested inside a suite of coarser resolution models. The high-resolution domain had a horizontal grid spacing of approximately 1 km and received hourly lateral boundary conditions from a 4 km model on a larger domain. The 4 km model was nested inside a 12 km domain, which was in turn driven by an N216 global model forecast. The 1 km grid was centred on (58.60° N, -6.45° W) with 1024 points East-to-West and 744 points North-to-South and a zonal and meridional grid spacing of 0.0135 degrees. The model time step was 50 s and the vertical level set comprised 70 levels, with a grid spacing of approximately 250 m at the altitudes of interest for this study.

The model is non-hydrostatic and employs the semi-Lagrangian advection scheme. In terms of model-physics, the model is broadly comparable to the version of Met Office operational UKV forecasting system that was used operationally until the autumn of 2011 (Lean et al., 2008). However, in an attempt to represent the simulated cloud system as well as possible, the following changes were made to the ice cloud micro-physics. Firstly, the ice particle size distribution (PSD) parameterisation was changed so as to be consistent with the PARASOL radiative retrievals (see Sect. 3 for details). Secondly, the mass-diameter relation of the ice crystals was taken directly from the Constrain in situ measurements (Cotton et al., 2013), and is therefore a “best-estimate” of this property for the simulated cloud system. For this paper, the NWP model was initialized at midnight on 25 January 2010, and the RH_i forecast field was extracted from the model on the same day but at the 13:00 UTC time step.

At about the same time as the NWP model RH_i field was extracted there was a PARASOL overpass at about 12:50 UTC. PARASOL has its central channels located at 0.443 μm , 0.490 μm , 0.565 μm , 0.670 μm , 0.763 μm , 0.765 μm , 0.865 μm , 0.910 μm and 1.02 μm . In this study, use is made of the instrument’s 0.865 μm channel, due to the

Scattering phase function of cirrus and the atmospheric state

A. J. Baran et al.

Title Page

Abstract

Introduction

Conclusions

References

Tables

Figures



Back

Close

Full Screen / Esc

Printer-friendly Version

Interactive Discussion



Scattering phase function of cirrus and the atmospheric state

A. J. Baran et al.

Title Page

Abstract

Introduction

Conclusions

References

Tables

Figures



Back

Close

Full Screen / Esc

Printer-friendly Version

Interactive Discussion



replicated one day of PARASOL cirrus observations of total reflectance, between the scattering angles of about 60° and 180° (Baran and Labonnote, 2007). It was further shown by Baran and Labonnote (2007) that the second randomised member of the ensemble model, randomized in such a way as to produce featureless scattering matrix elements, replicated one day of the global linear polarized reflectance measurements at close to cloud-top.

To demonstrate why the ensemble model can replicate in situ estimates of the volume extinction coefficient to within current experimental uncertainties, here the model predictions of the area ratio are compared against in situ estimates of naturally-occurring area ratios. The area ratio, A_r , is a useful measure of particle non-sphericity using in situ observations obtained from two-dimensional imaging probes. It is defined as the ratio of the projected area of a non-spherical particle to the area of a circumscribing circle of the same maximum dimension as the non-spherical particle. The averaged, $\langle A_r \rangle$, area ratio value predicted by each member of the ensemble is shown in Fig. 3, and in the figure, the predicted values are compared against in situ estimates of A_r . The in situ observations shown in Fig. 3 are obtained from a number of aircraft field campaigns that took place in the Arctic, mid-latitudes and tropics (Heymsfield and Miloshevich 2003; Field et al., 2008; McFarquhar et al., 2013). The A_r values from McFarquhar et al. (2013) were obtained in the Arctic at ice crystal maximum dimensions between about $35 \mu\text{m}$ and $60 \mu\text{m}$, and the averaged-values of $\langle A_r \rangle$ were reported to be between 0.65 to 0.58, but with a standard deviation of $\pm 45\%$. These averaged values were found for 80 % of the estimates compiled by McFarquhar et al. (2013). The in situ estimates of A_r from Heymsfield and Miloshevich (2003) are a synthesis of all the mid-latitude data (Eq. 2 from Heymsfield and Miloshevich 2003) compiled in that paper, and those estimates were prescribed an uncertainty of $\pm 50\%$ for ice crystals less than $3000 \mu\text{m}$, the uncertainty reducing to $\pm 25\%$, for sizes greater than $3000 \mu\text{m}$. The data from Field et al. (2008) were obtained in the tropics at ice crystal maximum dimensions between about $200 \mu\text{m}$ and $10000 \mu\text{m}$, and in Fig. 3, the upper and lower bounds on the data from Field et al. (2008) are shown, but on those bounds, there is

rently, the members of the ensemble model are distributed into six equal size intervals of the PSD. However, this distribution of the predicted area throughout the PSD can change, given further information on the most general weights to apply to the model.

In this study, the PSD assumed is the moment estimation parameterization of the PSD developed by Field et al. (2007), hereinafter referred to as F07. The F07 parameterization relates the 2nd moment (i.e., IWC) to any other moment via a polynomial fit to the in-cloud temperature. The parameterization is based on 10 000 in situ measurements of the PSD, and the measurements were filtered using the method of Field et al. (2006) to reduce artefacts of ice crystal shattering at the inlet of the microphysical probes (Korolev et al., 2011), and the PSD was truncated at an ice crystal maximum dimension of 100 μm . The in situ observations were obtained from the mid-latitudes and Tropics, at in-cloud temperatures between about -60°C and 0°C . The parameterization does not ignore ice crystals less than 100 μm , but assumes that these ice crystals follow an exponential PSD. For ice crystal sizes greater than 100 μm , the parameterization uses a gamma function, which was found to best-fit the in situ measured PSDs. The parameterization adds together the exponential and gamma function to reconstruct the full PSD, given the IWC and in-cloud temperature. It has been previously shown that the F07 parameterization is a good fit to in situ measurements of tropical and mid-latitude PSDs (Baran et al., 2011a; Furtado et al., 2013). Since the parameterization fundamentally relates the 2nd moment of the PSD to any other moment via the in-cloud temperature, to estimate representative PSDs, a mass-dimensional relationship is required. In this paper, the ensemble model predicted mass-dimensional relationship is used to generate the F07 PSDs. The ensemble model mass-dimensional relationship was previously derived by Baran et al. (2011b) and in that paper, it was shown that the ensemble model predicts that ice crystal mass of each particle is given by $0.04 D^2$, where D is the maximum dimension of each ice crystal, and the mass is in SI units. The ensemble model mass-dimensional relationship is within the upper uncertainty of the Constrain derived mass-dimensional relationship reported in Cotton et al. (2013), and it is therefore, representative of naturally-occurring ice crystal mass.

Scattering phase function of cirrus and the atmospheric state

A. J. Baran et al.

[Title Page](#)[Abstract](#)[Introduction](#)[Conclusions](#)[References](#)[Tables](#)[Figures](#)[Back](#)[Close](#)[Full Screen / Esc](#)[Printer-friendly Version](#)[Interactive Discussion](#)

3.1.1 The single-scattering properties

Incident unpolarized sunlight is assumed to irradiate a collection of randomly oriented non-spherical particles, each of which possesses a plane of symmetry. The single-scattering properties that are applied to the PARASOL measurements are calculated using the Monte-Carlo ray tracing method, which was developed and made generally available by Macke et al. (1996a). Each member of the ensemble is randomized, using the method of distortion, and maximum randomizations are achieved using distortion and embedding, within the volume of the ice crystals, spherical air bubbles (Shcherbakov et al., 2006). The method of distortion involves randomly tilting the normal vector to the surface of the ice crystal, at the ice-air interface, with respect to its original direction. In this way, at each refraction-reflection event, the directions of the ray paths are changed with respect to their original direction, with the result that featureless scattering matrix elements are predicted. The values of distortion can be between 0 and 1, where 0 represents unperturbed scattering matrix elements and these retain scattering features, such as halo and ice bows. As the distortion is increased to higher values, the optical features are removed, to produce featureless scattering matrix elements. The distortion method attempts to replicate the complex processes that may occur on and within ice crystals, which could lead to featureless phase functions. Other authors refer to distortion as “micro-scale surface roughness.” However, this description of surface roughness may not be accurate as surface roughness can take on different forms (Mason 1971; Pfalzgraff et al., 2010; Bacon et al., 2003; Malkin et al., 2012). For instance, a theoretical electromagnetic study by Liu et al. (2013) has shown that at high values of idealized surface roughness, the method of distortion does not accurately reproduce the scattering phase function. In this study, the method of distortion is merely used to randomize the ice crystal so that featureless scattering phase functions are produced.

Here the distortion parameter is assumed to have the values of 0, 0.15, 0.25 and 0.4. The distortion value of 0.4 is also combined with embedding the ice crystal with spher-

Scattering phase function of cirrus and the atmospheric state

A. J. Baran et al.

Title Page

Abstract

Introduction

Conclusions

References

Tables

Figures



Back

Close

Full Screen / Esc

Printer-friendly Version

Interactive Discussion



Scattering phase function of cirrus and the atmospheric state

A. J. Baran et al.

Title Page

Abstract

Introduction

Conclusions

References

Tables

Figures



Back

Close

Full Screen / Esc

Printer-friendly Version

Interactive Discussion



ical air bubbles, to achieve the maximum randomization of the ice crystals to produce featureless phase functions. The upper distortion value of 0.4 was chosen as this was found to best-fit one day of global POLDER-2 measurements of the total reflectance and linearly polarized reflectance (Baran and Labonnote, 2006). For the most randomized case of assuming a distortion value of 0.4 and including the ice crystal with spherical air bubbles, the phase functions are calculated using the modifications by Shcherbakov et al. (2006) applied to the ray tracing model of Macke et al. (1996a). The statistics describing the tilt angles were shown by Shcherbakov et al. (2006) to be best represented by using Weibull statistics, where the Weibull distribution is defined by the scale (i.e., the distortion as described above) and shape parameters. This finding was based on cloud chamber measurements of the angular scattered intensity from a collection of ice crystals, at a visible wavelength, and comparisons between measurements and ray-tracing results showed that the Weibull statistics were the better match to the measurements. Moreover, the choice of Weibull statistics is consistent with independent cloud chamber results found by Neshyba et al. (2013). For the most randomized case considered in this paper, the Weibull statistics are assumed to have the following scale and shape parameter values of 0.4 and 0.85, respectively, and for the spherical air bubble inclusions, a mean free path of 200 μm is assumed (Baran and Labonnote 2007). The chosen values describing the Weibull statistics are also consistent with the values derived from independent cloud chamber measurements reported in Neshyba et al. (2013).

To interpret the PARASOL measurements the scattering phase function is required. The bulk-averaged scattering phase function, $\langle P_{11}(\theta) \rangle$, is given by the following equation,

$$\langle P_{11}(\theta) \rangle = \frac{\int C_{\text{sca}}(\bar{q}) P_{11}(\theta, \bar{q}) n(\bar{q}) d\bar{q}}{\int C_{\text{sca}}(\bar{q}) n(\bar{q}) d\bar{q}} \quad (1)$$

where the vector (\bar{q}) in Eq. (1) represents the elements of the ensemble model as a function of maximum dimension, $n(\bar{q})$ is the F07 parametrized PSD, and $C_{\text{sca}}(\bar{q})$ is the

scattering cross-section of each of the ensemble model members. To generate the F07 PSDs, the IWC and in-cloud temperature are assumed to have the values of 0.01 gm^{-3} and -50°C , respectively.

The bulk-averaged asymmetry parameter, $\langle g \rangle$, is calculated using the following equation,

$$\langle g \rangle = \frac{\int g(\bar{q}) C_{\text{sca}}(\bar{q}) n(\bar{q}) d\bar{q}}{\int C_{\text{sca}}(\bar{q}) n(\bar{q}) d\bar{q}} \quad (2)$$

where the parameters in Eq. (2) have been previously defined. Another parameter of importance in calculating the total cloud reflectance is the single-scattering albedo, ω_0 , which is the ratio of the scattered radiation to that totally attenuated in the hemisphere of all directions. Here, the wavelength of $0.865 \mu\text{m}$ is considered, at such a weakly absorbing wavelength, the value of ω_0 will be close to unity.

The bulk-averaged volume extinction coefficient, $\langle \beta_{\text{ext}} \rangle$, is calculated from the following equation,

$$\langle \beta_{\text{ext}} \rangle = \int C_{\text{ext}}(\bar{q}) n(\bar{q}) d\bar{q} \quad (3)$$

where $C_{\text{ext}}(\bar{q})$ is the extinction cross-section of each member of the ensemble model, calculated as a function of its maximum dimension.

Figure 4 shows the bulk-averaged ensemble model predicted scattering phase functions, calculated at the wavelength of $0.865 \mu\text{m}$, assuming distortion values of 0, 0.15 (slightly distorted), 0.25 (moderately distorted), and 0.4 plus spherical air bubble inclusions (fully distorted with spherical air bubble inclusions). The complex refractive index of ice at $0.865 \mu\text{m}$ has the value of $1.304 + 2.400 \times 10^{-7}i$, where i is the imaginary part of the index (Warren and Brandt, 2008). The total optical properties (i.e., $\langle g \rangle$ and ω_0) are tabulated in Table 1 for each of the assumed ensemble models. Figure 5 shows the maximum contribution to the ice crystal scattering cross-section per particle, as a function of maximum dimension, assuming the IWC and in-cloud temperature values given

Scattering phase function of cirrus and the atmospheric state

A. J. Baran et al.

Title Page

Abstract

Introduction

Conclusions

References

Tables

Figures

◀

▶

◀

▶

Back

Close

Full Screen / Esc

Printer-friendly Version

Interactive Discussion



Scattering phase function of cirrus and the atmospheric state

A. J. Baran et al.

Title Page

Abstract

Introduction

Conclusions

References

Tables

Figures



Back

Close

Full Screen / Esc

Printer-friendly Version

Interactive Discussion



above. The figure shows that the maximum contribution to the scattering cross-section occurs at a maximum dimension of about $50\ \mu\text{m}$. Defining the size parameter, x , as $\pi D/\lambda$, where λ is the incident wavelength, gives a value of x of about 182. This value of x means that the Monte-Carlo ray-tracing method is within the range of x where the method is applicable (Yang and Liou 1996).

Figure 4 shows that as the distortion parameters are gradually increased, the halo and ice bow features gradually diminish, and for the most randomized case, the scattering phase function becomes featureless and almost flat at backscattering angles. At the scattering angles of relevance to this study, the figure shows that discrimination between the model phase functions should be possible using the viewing geometry of PARASOL.

To retrieve the total reflectance using PARASOL, a radiative transfer model is required, here the model developed by de Haan et al. (1986) is used and its application to PARASOL has been fully described by Labonnote et al. (2001). The radiative transfer model assumes a plane-parallel cloud, but it is fully inclusive of multiple scattering. Also taken into account are layers of aerosol below the cloud and Rayleigh scattering above and below the cloud is also taken into account. At the wavelength of $0.865\ \mu\text{m}$, the PARASOL retrieval algorithm assumes that the sea surface has a reflectance value of 0.000612 and a wind speed of $7\ \text{ms}^{-1}$; see Buriez et al. (2001) for further details about the PARASOL retrieval algorithm. In the next section, the retrieval methodology is described.

4 Methodology

The methodology of retrieving the Spherical albedo using PARASOL multi-directional measurements of total reflectance has been previously described by (Doutriaux-Boucher et al., 2000; Buriez et al., 2001; and Labonnote et al., 2001), but a brief description of the retrieval is given here. The total reflectance of the cloud is specified by the vertical volume extinction coefficient, the vertical extent of the cloud, and the

Scattering phase function of cirrus and the atmospheric state

A. J. Baran et al.

Title Page

Abstract

Introduction

Conclusions

References

Tables

Figures



Back

Close

Full Screen / Esc

Printer-friendly Version

Interactive Discussion



scattering phase function. The cloud optical depth is therefore given by the integral of the vertical extinction over the vertical depth of the cloud. Since the cloud is essentially over a non-reflecting surface, the only directional information is provided by the assumed scattering phase function. It has been previously shown by Doutriaux-Boucher et al. (2000) that there is a one-to-one relationship between the cloud optical depth and the cloud spherical albedo (i.e., integral of the plane albedo over all incoming directions, where the plane albedo is a function of solar zenith angle alone), if the surface below the cloud is black. The cloud optical depth is retrieved, under the assumption of a plane-parallel homogeneous layer, by matching the simulated cloud reflectance to the measured cloud reflectance at each scattering angle. If the phase function were a perfect representation of the cloud, then the retrieved cloud optical depth will be the same at each scattering angle. Therefore, the retrieved spherical albedo would also be the same at each scattering angle. If the assumed phase function were a poor representation of the cloud, then this would result in a directional dependence on the spherical albedo, which would be unphysical. This retrieval methodology forms the basis of this paper, and it has been applied by other studies that have utilized PARASOL measurements to test ice cloud scattering phase functions, see for example (Doutriaux-Boucher et al., 2000; Labonnote et al., 2001; Baran et al., 2001; Knapp et al., 2005; Baran and Labonnote 2006).

As previously stated, the retrievals of spherical albedo are performed on a pixel-by-pixel basis, and the data products derived from the PARASOL observations are only used if the following four conditions are met: (i) for each $6\text{ km} \times 6\text{ km}$ pixel the cloud fraction is unity, (ii) the total number of view angles ≥ 7 , (iii) the difference between the minimum and maximum sampled scattering angle is greater than 50° , and (iv) only pixels over the sea are considered. The total number of PARASOL pixels that meet these four conditions within the area of interest shown in Fig. 1 is 297. As previously stated, since, by definition, the true cloud spherical albedo is independent of direction, then for each pixel, the retrieved averaged directional spherical albedo, $\langle S \rangle$, should be identical to the directional spherical albedo, $S(\theta)$, where θ is the scattering angle, if

the model phase function were a perfect representation of the cloud. The retrievals of $S(\theta)$ depend on the assumed scattering phase function, the vertical volume extinction coefficient and ω_0 .

The averaged spherical albedo, $\langle S \rangle$, for each pixel is defined by,

$$\langle S \rangle = \frac{1}{N} \sum_{j=1}^{j=N} S_j(\theta) \quad (4)$$

where N is the total number of viewing directions, which for the case considered in this paper is between 7 and 8. To find the phase function that best minimizes the spherical albedo differences, the root mean square error (rmse) is found for each pixel, which is given by

$$\text{rmse} = \sqrt{\frac{\sum_{j=1}^N \Delta S^2}{N}} \quad (5)$$

where in Eq. (5), $\Delta S = \langle S \rangle - S(\theta)$, and the other terms have been previously defined.

In the sections that follow, the model phase functions shown in Fig. 4 and the total optical properties given in Table 1 are applied to the PARASOL measurements, on a pixel-by-pixel basis, to retrieve the phase function that best minimises Eq. (5). Results of this analysis are then used to explore possible relationships between ice crystal randomization and RH_i .

5 Results

5.1 Validating the NWP model field of RH_i

Before exploring the possible relationship between RH_i and the scattering phase function, it is first necessary to show that the NWP predicted field of RH_i is sufficiently

**Scattering phase
function of cirrus and
the atmospheric state**A. J. Baran et al.

[Title Page](#)[Abstract](#)[Introduction](#)[Conclusions](#)[References](#)[Tables](#)[Figures](#)[Back](#)[Close](#)[Full Screen / Esc](#)[Printer-friendly Version](#)[Interactive Discussion](#)

accurate for the purposes of this paper. Firstly, Fig. 6 shows the NWP model predicted water vapour mixing ratio field and the location of the PARASOL pixels, and the position of the aircraft within that field. The aircraft positions were predominantly located around the areas of semi-transparent cirrus, with no cloud beneath, as shown by Fig. 1.

5 Figure 6 shows that there is considerable variation in the water vapour field at about the cloud-top, around the North and East of Scotland. As a consequence of this variation, there will be a sufficient change in the RH_i field at the cloud-top as a function of position, to relate retrieval results to the model field. From Fig. 6 we note that the NWP model predicted the cloud-top to be in the vicinity of 10 km for the region of interest.

10 Figure 7 (a) shows the aircraft-mounted lidar estimate of the volume extinction coefficient as a function of altitude, and the bottom panel shows the derived lidar optical depth as a function of time. Figure 7a shows that the lidar estimated cloud-top altitude was at about 10 km, at approximately 13:21 UTC, which is in good agreement with the NWP model prediction.

15 To validate the NWP model prediction of the RH_i field use is now made of the aircraft-mounted ARIES measurements, which are applied to obtain retrievals of RH_i . The retrieval of RH_i from the ARIES measurements is achieved using the Havemann-Taylor Fast Radiative Transfer Code (HTFRTC) (Havemann 2006; Havemann et al., 2009) and the retrieval method of Thelen et al. (2012). Moreover, the ARIES-based retrieval

20 of RH_w (relative humidity with respect to water) is validated against the dropsonde measurements of RH_w . The HTFRTC is a principal component based radiative transfer model and is fully inclusive of the atmosphere and exact multiple scattering. The ARIES spectrum was averaged over 10 spectra and was de-noised using principal components, which act as a low-pass filter. For this case, European Centre for Medium-Range Weather Forecasting (ECMWF) atmospheric profiles are applied as the back-

25 ground state and the Optimal Estimation (OE) method of Rodgers (1976), is used, which is a Bayesian method. Here, OE is used to retrieve the most likely atmospheric state, and the method includes a rigorous treatment of error. The errors arise from the ARIES instrument itself and from the forward model, as well as from the ECMWF

Scattering phase function of cirrus and the atmospheric state

A. J. Baran et al.

Title Page

Abstract

Introduction

Conclusions

References

Tables

Figures



Back

Close

Full Screen / Esc

Printer-friendly Version

Interactive Discussion



model background fields. The treatment of error by OE assumes that the errors are described by a Gaussian distribution. Here the background errors in the temperature, RH and IWC are assumed to be typically ± 0.4 K, ± 10 %, and ± 50 %, respectively. Given the errors, ARIES measurements, and simulated measurements using HTFRTC, OE uses a minimization procedure to find the most likely atmospheric state that best describes the measurement set, given the retrieved parameters or state vector. Currently, the state vector in the HTFRTC retrieval method (Thelen et al., 2012) is composed of the temperature profile, the relative humidity profile, homogeneous cirrus IWC, surface temperature, and surface emissivity. The temperature and relative humidity profiles are retrieved at all 70 levels of the Met Office operational suite of models. The comparisons between the ARIES retrieval of RH_w and the dropsonde measurements are shown in Fig. 8a. The ARIES retrieval of RH_i and the NWP model prediction of RH_i are shown for two different locations in Fig. 8b and c.

Figure 8a shows that the ARIES-based retrieval of RH_w in the presence of cirrus is in good agreement with the dropsonde measurements at the altitude of the cloud, where the retrievals are represented by the plus signs. The two different colours represent the retrievals based on the two different aircraft runs above the cirrus that were previously described. Each of the runs was 10 min in length. There were approximately eight ARIES retrievals per run. Figure 8b shows the ARIES-based retrieval of RH_i at the latitude 57.97° N and the longitude 3.195° W, which corresponds to the lower left of Fig. 6. The full line in the figure represents the NWP model predicted RH_i profile, and the retrievals are represented by the plus signs. The figure shows that the NWP model represents the vertical structure of RH_i rather well, with little deviation from the retrievals. The model and retrievals show values of RH_i reaching values of about 120 %. Figure 8c shows the same as Fig. 8b but at the latitude of 59.14° N and longitude 3.84° W, which corresponds to the upper left of Fig. 6. Figure 8c shows a similar result to Fig. 8b, but interestingly the model and retrieved RH_i , at this particular location, are less than 100 %. At a pressure of 1.50×10^4 Pa, there is a spike in the model RH_i field, but this is not supported by the retrievals and is probably due to numerical instability

Scattering phase function of cirrus and the atmospheric state

A. J. Baran et al.

Title Page

Abstract

Introduction

Conclusions

References

Tables

Figures



Back

Close

Full Screen / Esc

Printer-friendly Version

Interactive Discussion



and moderately distorted (distortion = 0.25) ensemble model phase functions, respectively. Therefore, the results shown in Fig. 9 (a) indicate that on a pixel-by-pixel basis, the most randomized ice crystal model phase functions may not always be the best-fit to multi-angular total reflectance measurements. It is interesting to note here that, for the same pixels, the rmse values found for the 12 pixels with less randomized phase functions were on average about $\frac{3}{5}$ of the rmse values found for the most randomized phase functions.

Clearly, in the upper left-hand side of Fig. 9a, there must have been sufficiently strong backscattering features present in the spherical albedo measurements to discriminate between the most randomized and least randomized phase functions. Furthermore, Baran et al. (2012) also found that, for a case of mid-latitude, very high IWC anvil cirrus at near to cloud-top, the PN measured averaged scattering phase function also exhibited strong backscattering features. Clearly, such findings of optical features on the scattering phase function of naturally-occurring ice crystals indicate the need for radiometric or in situ observations to sample the scattered angular intensities over a more complete range of scattering angle than is currently possible. Measuring the forward and backscattering intensities alone is not sufficiently general (Baran et al., 2012). However, the most common retrievals shown in Fig. 9a are representative of the most randomized ice crystals and these have featureless phase functions. For the purposes of retrieving cirrus properties using global radiometric measurements, it is most likely that featureless phase functions are still generally better at representing cirrus radiative properties than their purely pristine counterparts (Foot 1988; Baran et al., 1999, 2001; Baran and Labonnote, 2006; Baum et al., 2011; Cole et al., 2013; Ulanowski et al., 2013).

It is also of interest to note the change in the asymmetry parameter values shown in Table 1. From the pristine ensemble model phase function to the most randomized ensemble model phase function the change in the asymmetry parameter is about 5%. A change in the asymmetry parameter of 5% is radiatively important as illustrated by the following example. Given that the instantaneous solar irradiance arriving at the Earth's

**Scattering phase
function of cirrus and
the atmospheric state**

A. J. Baran et al.

Title Page

Abstract

Introduction

Conclusions

References

Tables

Figures



Back

Close

Full Screen / Esc

Printer-friendly Version

Interactive Discussion



top-of-atmosphere is about 1370 Wm^{-2} . Under the assumptions of conservative scattering and a dark ocean below the cirrus, a change of 5% in the asymmetry parameter results in a difference of about 43 Wm^{-2} in the reflected solar irradiance back to space. This difference of 43 Wm^{-2} is very significant with regard to the energetics of the Earth's atmosphere, and indicates why it is important to globally constrain values of the asymmetry parameter (Baran, 2012; Ulanowski et al., 2013; Van de Diedenhoven et al., 2013).

Shown in Fig. 9b is the NWP model predicted RH_i field at a cloud-top altitude of 10 km. On comparison with Fig. 9a, it can be seen from Fig. 9b, that the most randomized phase functions (i.e, yellow squares) correspond to model pixels with $\text{RH}_i > 100\%$. Conversely, the 12 pixels that are best represented by the pristine, slightly or moderately distorted phase functions correspond to NWP model pixels with $\text{RH}_i \sim \leq 100\%$. Interestingly, at the cloud-top, there is a clear correlation between the NWP model RH_i field and the estimated ice crystal randomization. This correlation is demonstrated by Fig. 10. In that figure, the -500 values represent the pristine ice crystals (distortion=0), whilst the values of 1000 represent the most randomized phase functions (distortion = 0.4 with spherical air bubble inclusions). The slightly distorted and moderately distorted ensemble model phase functions are represented by the values of 0 and 500, respectively. The results presented in Fig.10 are broadly consistent with the findings of Gayet et al. (2011), which showed that the 22° halo feature was associated with $\text{RH}_i \leq 100\%$, whilst featureless phase functions were associated with $\text{RH}_i > 100\%$.

Although the results presented in Fig. 10 demonstrate that, at least for this case and at the cloud-top, there is a correlation between the NWP RH_i field and ice crystal randomization. However, this correlation intrinsically assumes that the PARASOL cloud spherical albedo measurements occur at the cloud-top. In reality, solar radiation at $0.865 \mu\text{m}$ will penetrate to some depth within the cloud layer, and this depth of penetration needs to be calculated to test whether the assumption of cloud-top penetration is correct.

Scattering phase function of cirrus and the atmospheric state

A. J. Baran et al.

Title Page

Abstract

Introduction

Conclusions

References

Tables

Figures



Back

Close

Full Screen / Esc

Printer-friendly Version

Interactive Discussion



To calculate the depth of penetrating radiation at $0.865\ \mu\text{m}$, a Monte-Carlo radiative transfer model has been used to represent the cirrus layer of relevance to this study. The Monte-Carlo model used here is fully described by Cornet al. (2009). A description of the Monte-Carlo model set-up and definition of the probability of penetration is given in Appendix A. The percent probability of penetration as a function of cloud depth, and optical depth is shown in Fig. 11a and b. Results are shown in the figure for the backscattered and forward scattered radiation in the solar plane, respectively.

It should be noted here that the PARASOL retrievals of optical depth were generally greater than about 1, which is consistent with the independently derived lidar optical depth shown in Fig. 7b. The average value of the lidar optical depth was found to be about 1.2. The lidar vertical profiles of optical depth were obtained when the aircraft was located above the cirrus, at an altitude of almost 11 km, which occurred during the times shown in the figure. There is a gap of about three minutes shown in Fig. 7b, which is the time required for the aircraft to turn and commence the second straight and level run.

Figure 11a and b shows that by a depth of 1 km from the cloud-top, the probability of penetration has been approximately halved, for optical depths greater than 0.3. By 1.5 km from the cloud-top, the probability of penetration is generally less than 40 %. The percent probability of penetration shown in Fig. 11a and b is similar. This is because the scattering phase function used in the Monte-Carlo calculations, at backscattering angles, is largely invariant with respect to the scattering angle. This is simply because the scattering phase functions representing the most randomised ice crystals are flat and featureless at backscattering angles.

From Fig. 11a and b, it can be concluded that the PARASOL measurements of the total reflectance is biased towards the cloud-top, but they are not solely relatable to the cloud-top. Therefore, to compare the NWP model RH_i field against the estimated ice crystal randomization, the model field must be weighted, to obtain the vertically averaged model RH_i field, which can then be compared against the estimated ice crystal randomization. The vertical resolution of the NWP model is about 250 m, at

5 cirrus altitudes, and it can be seen from Fig. 11a and b that the weightings towards the cloud-top should clearly have the largest values. The number of model layers within 1.5 km of the cloud top, which is the distance from within the cloud where most of the reflected radiation originates, is about 5. The weightings applied to obtain the vertically averaged model RH_i field were assumed to have the following values of 0.6, 0.3, 0.07, 0.02, and 0.01. The resulting correlation between the vertically-averaged NWP model RH_i field and estimated ice crystal randomization is shown in Fig. 12.

10 The figure shows that even after vertically-averaging the RH_i field, there is still a discernible correlation between RH_i and ice crystal randomization, which is not significantly different from that shown in Fig. 10. The results presented in Fig. 12 do seem to suggest that there should be a correlation between ice crystal randomization and RH_i . The results presented within this paper are consistent with the in situ measurements of Gayet et al. (2011) and the laboratory studies of Ulanowski et al. (2013). Clearly, this paper has demonstrated that space-based remote sensing can also be used to investigate relationships between scattering properties of ice crystals and atmospheric state parameters. If more general correlations can be found between the asymmetry parameter and the atmospheric state, then this will have important implications for parameterization of the asymmetry parameter in climate models, since then, g would become a function of RH_i and temperature.

20 Climate model parameterizations of the asymmetry parameter are currently assumed to be invariant with respect to atmospheric state variables. It is desirable, as argued by Baran et al. (2014b), Baran (2012) and by Baran et al. (2009), to relate general circulation model prognostic variables directly to ice optical properties, so that the prognostic variables can then be directly related to space-based radiometric measurements. Only through directly relating general circulation model prognostic variables to radiative measurements can the possibility of error cancellation be removed from within climate models.

Scattering phase function of cirrus and the atmospheric state

A. J. Baran et al.

[Title Page](#)[Abstract](#)[Introduction](#)[Conclusions](#)[References](#)[Tables](#)[Figures](#)[Back](#)[Close](#)[Full Screen / Esc](#)[Printer-friendly Version](#)[Interactive Discussion](#)

**Scattering phase
function of cirrus and
the atmospheric state**

A. J. Baran et al.

Title Page

Abstract

Introduction

Conclusions

References

Tables

Figures



Back

Close

Full Screen / Esc

Printer-friendly Version

Interactive Discussion



ment with the NWP predicted vertical profile of RH, for two very different locations within the cirrus field. Moreover, the NWP model prediction of cloud-top, vertical depth, and cloud-base were shown to be consistent with lidar measurements of the same quantities. Assuming that the NWP RH_i fields are representative of truth, the model fields were directly related to the remote sensing observations of ice crystal randomization.

A positive correlation is reported, between ice crystal randomization and RH_i . That is, featureless phase functions, representing highly randomized ice crystals, were shown to be associated with $RH_i > 100\%$. However, phase functions representing pristine ice crystals were found to be associated with $RH_i \sim \leq 100\%$. The positive correlation between RH_i and ice crystal randomization still persisted even after obtaining a weighted-average of the NWP RH_i field, to take into account the penetration depth of solar radiation at the wavelength of $0.865\ \mu\text{m}$.

The findings of this paper may have implications for the parameterization of the asymmetry parameter in climate models. This is because, if the relationships reported above are shown to be robust, then the asymmetry parameter should be parametrized as functions of model prognostic variables. This means that in regions of high and low RH_i , the g -values will naturally vary according to the complexity of ice crystals.

Currently, climate model parameterizations of g do not take into account the changing atmospheric state. Such a change in the asymmetry parameter could lead to differences of some $43\ \text{Wm}^{-2}$ in the instantaneous value of the short-wave radiation reflected back to space at the top-of-atmosphere. Clearly, such large radiative differences need to be constrained.

To obtain such a constraint, many in situ and remotely sensed measurements of the light scattering properties of ice crystals are required, as a function of RH_i and cloud temperature, from a large number of globally distributed cirrus cases, using instrumentation previously discussed in Gayet et al., 2011, Ulanowski et al., 2013, and Van de Diedenhoven et al., 2013. This paper has demonstrated the need for such large-scale measurements. Preferably, new in situ instrumentation should be developed that is ca-

pable of measuring the scattered intensities over a larger range of scattering angle than is currently possible (Baran et al., 2012).

Appendix A:

The radiative transfer model assumes a plane-parallel layer, with a vertical extent of 3 km. This cloud depth is consistent with the lidar result shown in Fig. 7a. The vertical resolution of the cloud layer is assumed to be 0.1 km, and the cloud-top is situated at an altitude of 10 km, which is also consistent with the lidar result shown in Fig. 7a. The relevant solar-satellite geometry for this case has been applied to the Monte-Carlo calculations. That is, the solar zenith angle is 75° . The view angle of PARASOL at the time of the overpass has an average value of 50° . The standard deviation of the PARASOL view angle is generally less than 2° . For the purposes of this study, an average view angle will suffice. The view angle used in the Monte-Carlo model was set to a value of 49.35° . Moreover, the PARASOL azimuth angle did not vary significantly and the standard deviation of this angle was no more than 4.5° . With little variation in the satellite geometry, the Monte-Carlo calculations have been performed in the solar plane to obtain the most general results. This means that $\varphi - \varphi_0 = 0$ for forward scattered radiation, and $\varphi - \varphi_0 = 180^\circ$ for backscattered radiation, in the principal plane, where φ and φ_0 are defined as the satellite and solar azimuth angles, respectively. The cloud microphysical model is assumed to be the most randomized ensemble model phase function, which was the most common retrieval shown in Fig. 9a, and the values of the volume extinction coefficient and single-scattering albedo were taken from Table 1. The probability of penetration is calculated by computing the total distance the ray travels within each sub-layer of the cloud. From this analysis, a PDF of penetration is obtained, which is normalized to unity, from which the percent probability of penetration is easily calculated as a function of distance from the cloud-top.

Scattering phase function of cirrus and the atmospheric state

A. J. Baran et al.

Title Page

Abstract

Introduction

Conclusions

References

Tables

Figures



Back

Close

Full Screen / Esc

Printer-friendly Version

Interactive Discussion



Acknowledgements. The BAe-146 aircrew, Direct Flight operations staff, FAAM and FGAM instrument operators are thanked for their assistance during the flight. The Facility for Airborne Atmospheric Measurements is owned by the Met Office and the Natural Environment Research Council. The image shown in Fig. 1 is kindly reproduced with permission from the NERC Satellite Receiving Station, Dundee University, Scotland (<http://www.sat.dundee.ac.uk/>).

References

- Bacon, N. J., Baker, M. B., and Swanson, B. D.: Initial stages in the morphological evolution of vapour-grown ice crystals: A laboratory investigation, *Q. J. Roy. Meteor. Soc.*, 129, 1903–1927, 2003.
- Bailey, M. and Hallett, J.: Growth rates and habits of ice crystals between -20°C and -70°C , *J Atmos. Sci.*, 61, 514–554, 2004.
- Bailey, M. and Hallett, J. A comprehensive habit diagram for atmospheric ice crystals: Confirmation from the laboratory, AIRS II, and other field campaigns, *J. Atmos. Sci.*, 66, 2888–2899, 2009.
- Baran, A. J.: From the single-scattering properties of ice crystals to climate prediction: A way forward. *Atmos Res.*, 112, 45–69, 2012.
- Baran, A. J. and Labonnote, L.-C.: On the reflection and polarisation properties of ice cloud, *J. Quant. Spectrosc. Radiat. Transfer.*, 100, 41–54, 2006.
- Baran, A. J. and Labonnote, L.-C.: A self-consistent scattering model for cirrus. 1: The solar Region, *Q. J. Roy. Meteor. Soc.*, 133, 1899–1912, 2007.
- Baran, A. J., Watts, P. D., and Francis, P. N.: Testing the coherence of cirrus microphysical and bulk properties retrieved from dual-viewing multispectral satellite radiance measurements, *J. Geophys. Res.*, 104, 31673–31684, 1999.
- Baran, A. J., Francis, P. N., Labonnote, L.-C., and Doutriaux-Boucher, M.: A scattering phase function for ice cloud: Tests of applicability using aircraft and satellite multi-angle multiwavelength radiance measurements of cirrus, *Q. J. Roy. Meteor. Soc.*, 127, 2395–2416, 2001.
- Baran, A. J., Connolly, P. J., and Lee, C.: Testing an ensemble model of cirrus ice crystals using mid-latitude in situ estimates of ice water content, volume extinction coefficient, and the total solar optical depth, *J. Quant. Spectrosc. Radiat. Transfer.*, 110, 1579–1598, 2009.

Scattering phase function of cirrus and the atmospheric state

A. J. Baran et al.

Title Page

Abstract

Introduction

Conclusions

References

Tables

Figures



Back

Close

Full Screen / Esc

Printer-friendly Version

Interactive Discussion



Scattering phase function of cirrus and the atmospheric state

A. J. Baran et al.

Title Page

Abstract

Introduction

Conclusions

References

Tables

Figures



Back

Close

Full Screen / Esc

Printer-friendly Version

Interactive Discussion



- Baran, A. J., Connolly, P. J., Heymsfield, A. J., and Bansemmer, A.: Using in situ estimates of ice water content, volume extinction coefficient, and the total solar optical depth obtained during the tropical ACTIVE campaign to test an ensemble model of cirrus ice crystals, *Q. J. Roy. Meteor. Soc.*, 137, 199–218, 2011a.
- 5 Baran, A. J., Bodas-Salcedo, A., Cotton, R., and Lee, C.: Simulating the equivalent radar reflectivity of cirrus at 94 GHz using an ensemble model of cirrus ice crystals: a test of the Met office global numerical weather prediction model, *Q. J. Roy. Meteor. Soc.*, 137, 1547–1560, 2011b.
- Baran, A. J., Gayet, J.-F., and Shcherbakov, V.: On the interpretation of an unusual in-situ measured ice crystal scattering phase function, *Atmos. Chem. Phys.*, 12, 9355–9364, doi:10.5194/acp-12-9355-2012, 2012.
- Baran, A. J., Cotton, R., Furtado, K., Havemann, S., Labonnote, L.-C., Marengo, F., Smith, A., and Thelen, J.-C.: A self-consistent scattering model for cirrus. Part II: The high and low frequencies, *Q. J. Roy. Meteor. Soc.*, 140, 1039–1057, 2014a.
- 15 Baran, A. J., Hill, P., Furtado, K., Field, P., and Manners, J: A coupled cloud physics-radiation parameterization of the bulk optical properties of cirrus and its impact on the Met Office unified global atmosphere 5.0 configuration, submitted to *J. Climate*, 2014b.
- Barrett, J. W., Garcke, H., and Numberg, R.: Numerical computations of faceted pattern formation in snow crystal growth, *Phys. Rev.*, E86, 011604, doi:10.1103/PhysRevE.86.011604, 2012.
- 20 Baum, B. A., Yang, P., Heymsfield, A. J., Schmitt, C. G., Xie, Y., Bansemmer, A., Hu, Y.-X., and Zhang, Z.: Improvements in Shortwave Bulk Scattering and Absorption Models for the Remote Sensing of Ice Clouds, *J. Appl. Meteor. Climatol.*, 50, 1037–1056, 2011.
- Buriez, J.-C., Doutriaux-Boucher, M., Parol, F., and Loeb, N. J.: Angular Variability of the Liquid Water Cloud Optical depth Retrieved from ADEOS-POLDER, *J. Atm. Sci.*, 58, 3007–3018, 2001.
- 25 Cole, B. H., Yang, P., Baum, B. A., Riedi, J., Labonnote, L.-C., Thieuleux, F., and Platnick, S.: Comparison of PARASOL Observations with Polarized Reflectances Simulated Using Different Ice Habit Mixtures, *J. Appl. Meteor. Climatol.*, 52, 186–196, 2013.
- 30 Cornet, C., Labonnote, L. C., and Szczap, F.: Three-dimensional Polarized Monte-Carlo Atmospheric Radiative Transfer Model (3DMCPOL): 3D Effects on Polarized Visible Reflectances of a Cirrus Cloud, *J. Quantit. Spectros. Radiativ. Trans.*, 111, 174–186, 2009.

Scattering phase function of cirrus and the atmospheric state

A. J. Baran et al.

Title Page

Abstract

Introduction

Conclusions

References

Tables

Figures



Back

Close

Full Screen / Esc

Printer-friendly Version

Interactive Discussion



- Cotton, R. J., Field, P. R., Ulanowski, Z., Kaye, P. H., Hirst, E., Greenaway, R. S., Crawford, I., Crosier, J., and Dorsey, J.: The effective density of small ice particles obtained from in situ aircraft observations of mid-latitude cirrus, *Q. J. Roy. Meteor. Soc.*, 139, 1923–1934, 2013.
- de Haan, J. F., Bosma, P. B., and Hovenier, J. W.: The adding method for multiple scattering calculations of polarized light, *Astron. Astrophys.*, 183, 371–391, 1986.
- Doutriaux-Boucher, M., Buriez, J. C., Brogniez, G., Labonnote, L.-C., and Baran, A. J.: Sensitivity of retrieved POLDER directional cloud optical depth to various ice particle models, *Geophys. Res. Lett.*, 27, 109–112, 2000.
- Fernald, F. G.: Analysis of atmospheric lidar observations: Some comments, *Appl. Opt.*, 23, 652–653, 1984.
- Field, P. R., Baran, A. J., Kaye, P. H., Hirst, E., and Greenway, R.: A test of cirrus ice crystal scattering phase functions. *Geophys. Res. Lett.*, 30, 1752, doi:10.1029/2003GL017482, 2003.
- Field, P. R., Heymsfield, A. J., Bansemer, A.: Shattering and Particle Interarrival Times Measured by Optical Array Probes in Ice Clouds. *J. Atmos. Ocean. Technol.*, 23, 1357–1371, 2006.
- Field, P. R., Heymsfield, A. J., and Bansemer, A.: Snow size distribution parameterization for midlatitude and tropical ice cloud. *J. Atmos. Sci.*, 64, 4346–4365, 2007.
- Field, P. R., Heymsfield, A. J., and Bansemer, A.: Determination of the combined ventilation factor and capacitance for ice crystal aggregates from airborne observations in a tropical anvil cloud.: *J. Atmos. Sci.*, 65, 376–391, 2008.
- Foot, J. S.: Some observations of the optical properties of clouds – II: Cirrus, *Q. J. Roy. Meteor. Soc.*, 114, 145–164, 1988.
- Furtado, K., Field, P. R., Cotton, R., and Baran, A. J.: The effects of ice crystal fall speed and particle size distribution on the simulation of high cloud, *Q. J. Roy. Meteor. Soc.*, submitted, 2014.
- Garrett, T. J., Gerber, H., Baumgardner, D. G., Thohy, C. H., and Weinstock, E. M.: Small highly reflective ice crystals in low-latitude cirrus, *Geophys. Res. Lett.*, 30, 10–13, 2003.
- Gayet, J. F., Crépel, O., Fournol, J. F., and Oshchepkov, S.: A new airborne polar Nephelometer for the measurements of optical and microphysical cloud properties. Part I: Theoretical design, *Ann. Geophys.*, 15, 451–459, doi:10.1007/s00585-997-0451-1, 1997.
- Gayet, J.-F., Asano, S., Yamazaki, A., Uchiyama, A., Sinyuk, A., Jourdan, O., and Aurol, F.: Two case studies of winter continental-type water and mixed-phase stratocu-

**Scattering phase
function of cirrus and
the atmospheric state**

A. J. Baran et al.

Title Page

Abstract

Introduction

Conclusions

References

Tables

Figures



Back

Close

Full Screen / Esc

Printer-friendly Version

Interactive Discussion



multi over the sea: 1. Microphysical and optical properties. *J. Geophys. Res.*, 107, 4569, doi:10.1029/2001JD001106, 2002.

Gayet, J.-F., Mioche, G., Shcherbakov, V., Gourbeyre, C., Busen, R., and Minikin, A.: Optical properties of pristine ice crystals in mid-latitude cirrus clouds: a case study during CIRCLE-2 experiment, *Atmos. Chem. Phys.*, 11, 2537–2544, doi:10.5194/acp-11-2537-2011, 2011.

Guignard, A., Stubenrauch, C. J., Baran, A. J., and Armante, R.: Bulk microphysical properties of semi transparent cirrus from AIRS: a six years global climatology and statistical analysis in synergy with CALIPSO and CloudSat, *Atmos. Chem. Phys.*, 12, 503–525, doi:10.5194/acp-12-503-2012, 2012.

Hallett, J., and Mason, B. J.: The influence of temperature and supersaturation on the habit of ice crystals grown from the vapor, *Proc Roy Soc Lon.*, A247, 440–453, 1958.

Havemann, S.: The development of a fast radiative transfer model based on an Empirical Orthogonal Functions (EOF) technique, *Proc. SPIE Int. Soc. Opt. Eng.*, 6405, 64050, doi:10.1117/12.693995, 2006.

Havemann, S., Thelen, J. C., Taylor, J. P., and Keil, A.: The Havemann-Taylor Fast Radiative Transfer Code: Exact fast radiative transfer for scattering atmospheres using Principal Components (PCs), In *AIP Conf. Proc.*, 1100, 38–40, doi:10.1063/1.3117000, 2009.

Heymsfield, A. J.: Precipitation development in stratiform ice clouds: A microphysical and dynamical study, *J. Atmos. Sci.*, 34, 367–381, 1977.

Heymsfield, A. J., and Miloshevich, L. M.: Parameterizations for the cross-sectional area and extinction of cirrus and stratiform ice cloud particles, *J. Atmos. Sci.*, 60, 936–956, 2003.

Intergovernmental Panel on Climate Change. *Climate Change 2013 – The Physical Science Basis*, Contribution of Working Group I to the fifth Assessment Report of the IPCC, Cambridge: Cambridge University Press, 1535 pp., 2013.

Jourdan, O., Oshchepkov, S., Shcherbakov, V., Gayet, J.-F., and Isaka, H.: Assessment of cloud optical parameters in the solar region: Retrievals from airborne measurements of scattering phase functions, *J. Geophys. Res.*, 108, 4572, doi:10.1029/2003JD003493, 2003.

Klett, J. D.: Lidar inversion with variable backscatter/extinction ratios. *Appl. Opt.*, 24, 1638–1643, 1985.

Knapp, W. H., Labonnote, L.-C., Brogniez, G., and Stammes, P.: Modeling total and polarized reflectances of ice clouds: Evaluation by means of POLDER and ATSR-2 measurements, *Appl. Opt.*, 44, 4060–4073, 2005.

Scattering phase function of cirrus and the atmospheric state

A. J. Baran et al.

Title Page

Abstract

Introduction

Conclusions

References

Tables

Figures



Back

Close

Full Screen / Esc

Printer-friendly Version

Interactive Discussion



- Korolev, A. V., Emery, E. F., Strapp, J. W., Cober, S. G., Isaac, G. A., Wasey, M., and Marcotte, D.: Small ice particles in tropospheric clouds: fact or artefact? Airborne icing instrumentation evaluation experiment, *B. Am. Meteor. Soc.*, 92, 967–973, 2011.
- Krämer, M., Schiller, C., Afchine, A., Bauer, R., Gensch, I., Mangold, A., Schlicht, S., Spelten, N., Sitnikov, N., Borrmann, S., de Reus, M., and Spichtinger, P.: Ice supersaturations and cirrus cloud crystal numbers, *Atmos. Chem. Phys.*, 9, 3505–3522, doi:10.5194/acp-9-3505-2009, 2009.
- Labonnote, L.-C., Brogniez, G., Buriez, J. C., Doutriaux-Boucher, M., Gayet, J. F., and Macke, A.: Polarized light scattering by inhomogeneous hexagonal monocrystals: Validation with ADEOS POLDER measurements, *J. Geophys. Res.*, 106, 12139–12153, 2001.
- Lean, H. W., Clark, P. A., Mark, D., Dixon, M., Roberts, N. M., Fitch, A., Forbes, A., and Halliwell, C.: Characteristics of high-resolution versions of the Met Office Unified Model for forecasting convection over the United Kingdom, *Mon. Weather Rev.*, 136, 3408–3424, 2008.
- Liou, K. N.: Influence of cirrus clouds on weather and climate: A global perspective, *Mon Weather Rev.*, 114, 1167–1199, 1986.
- Liu, C., Panetta, R. L., and Yang, P.: The effects of surface roughness on the scattering properties of hexagonal columns with sizes from the Rayleigh to the geometric optics regimes, *J. Quant. Spectrosc. Radiat. Transfer.*, 129, 169–185, 2013.
- Lynch, D. K., Sassen, K., O’C Starr, D., and Stephens, G.: *Cirrus*, Oxford, Oxford University Press, 504 pp., 2002.
- McFarquhar, G. M., Um, J., and Jackson, R.: Small cloud particle shapes in mixed-phase clouds, *J. Appl. Meteor. Climat.*, 52, 1277–1293, 2013.
- Macke, A., Mueller, J., and Raschke, E.: Single scattering properties of atmospheric ice crystal. *J. Atmos. Sci.*, 53, 2813–2825, 1996a.
- Macke, A., Mishchenko, M. I., and Cairns, B.: The influence of inclusions on light scattering by large particles, *J. Geophys. Res.*, 101, 23311–23316, 1996b.
- Malkin, T. L., Murray, B. J., Brukhno, A. V., Anwar, J., and Salzmann, C. G.: The structure of ice crystallised from supercooled water, *P. Natl. Acad. Sci. USA*, 109, 1041–1045, 2012.
- Marenco, F., Johnson, B., Turnbull, K., Newman, S., Haywood, J., Webster, H., and Ricketts, H.: Airborne lidar observations of the 2010 Eyjafjallajökull volcanic ash plume, *J. Geophys. Res.*, 116, D00U05, doi:10.1029/2011JD016396, 2011.
- Marshall, J. S. and Langleben, M. P.: A theory of snow-crystal habit and growth, *J. Meteorol.*, 11, 254–256, 1954.

Scattering phase function of cirrus and the atmospheric state

A. J. Baran et al.

[Title Page](#)[Abstract](#)[Introduction](#)[Conclusions](#)[References](#)[Tables](#)[Figures](#)[Back](#)[Close](#)[Full Screen / Esc](#)[Printer-friendly Version](#)[Interactive Discussion](#)

Mason B. J.: The physics of clouds, 2nd Ed, Oxford, Clarendon Press, 671 pp., 1971.

Mauno, P., McFarquhar, G. M., Räisänen, P., Kahnert, M., Timlin, M. S., and Nousiainen, T.: The influence of observed cirrus microphysical properties on shortwave radiation: A case study over Oklahoma, *J. Geophys. Res.*, 116, D22208, doi:10.1029/2011JD016058, 2011.

5 Muinonen, K.: Light scattering by non-spherical particles, San Diego, CA Academic Press, 323–349, 2000.

Nakaya, U.: Snow crystals. Cambridge, Harvard University Press, 510 pp., 1954.

Neshyba, S. P., Lowen, B., Benning, M., Lawson, A., and Rowe, P. M.: Roughness metrics of prismatic facets of ice, *J. Geophys. Res.*, 118, 3309–3318, 2013.

10 Nousiainen, T., Lindqvist, H., McFarquhar, G. M., and Um, J.: Small irregular ice crystals in tropical cirrus, *J. Atmos. Sci.*, 68, 2614–2627, 2011.

Pfalzgraff, W. C., Hulscher, R. M., and Neshyba, S. P.: Scanning electron microscopy and molecular dynamics of surfaces of growing and ablating hexagonal ice crystals, *Atmos. Chem. Phys.*, 10, 2927–2935, doi:10.5194/acp-10-2927-2010, 2010.

15 Platnick, S, King, M. D., Ackerman, S. A., Menzel, W. P., Baum, B. A., Riedi, J. C., and Frey, R. A.: The MODIS cloud products: Algorithms and examples from Terra, *IEEE Trans. Geosci. Remote Sens.*, 41, 459–473, 2003.

Rodgers, C. D.: Retrieval of Atmospheric Temperature and Composition From Remote Measurements of Thermal Radiation, *Rev. Geophys. Space Phys.*, 14, p. 609, 1976.

20 Schmitt, C. G. and Heymsfield, A. J.: The dimensional characteristics of ice crystal aggregates from fractal geometry, *J. Atmos. Sci.*, 67, 1605–1616, 2010.

Shcherbakov, V., Gayet, J.-F., Baker, B., and Lawson, P.: Light scattering by single natural ice crystals. *J. Atmos. Sci.*, 63, 1513–1525, 2006.

Shcherbakov, V.: Why the 46°halo is seen far less often than the 22°halo?, *J. Quantit. Spectr. Rad. Transf.*, 124, 37–44, 2013.

25 Stephens, G. L. and Webster, P. J.: Clouds and Climate: Sensitivity of Simple Systems, *J. Atmos. Sci.*, 38, 235–245, 1981.

Thelen, J. C., Havemann S, and Taylor J. P.: Atmospheric correction of short-wave hyperspectral imagery using a fast, full-scattering 1Dvar retrieval scheme, In Algorithms and Technologies for Multispectral, Hyperspectral, and Ultraspectral Imagery XVIII, edited by: Shen, S. S. and Lewis, P. E., *Proc. SPIE*, 8390, 839010, doi:10.1117/12.918012, 2012.

30 Ulanowski, Z., Hesse, E., Kaye, P. H., and Baran, A. J.: Light scattering by complex ice-analog crystals, *J. Quant. Spectrosc. Radiat. Transfer.*, 100, 382–392, 2006.

Scattering phase function of cirrus and the atmospheric state

A. J. Baran et al.

Table 1. The bulk values of $\langle \beta_{\text{ext}} \rangle$, $\langle \omega_0 \rangle$ and $\langle g \rangle$, calculated at the wavelength $0.865 \mu\text{m}$, for each distortion, assumed to have values of 0, 0.15, 0.25, and 0.4 plus spherical air bubble inclusions (Full), respectively.

Distortion	$\langle \beta_{\text{ext}} \rangle \text{km}^{-1}$	$\langle \omega_0 \rangle$	$\langle g \rangle$
0.0	0.506	0.99996	0.820
0.15	0.506	0.99990	0.813
0.25	0.506	0.99996	0.808
Full	0.506	0.99996	0.789

[Title Page](#)
[Abstract](#)
[Introduction](#)
[Conclusions](#)
[References](#)
[Tables](#)
[Figures](#)
[Back](#)
[Close](#)
[Full Screen / Esc](#)
[Printer-friendly Version](#)
[Interactive Discussion](#)

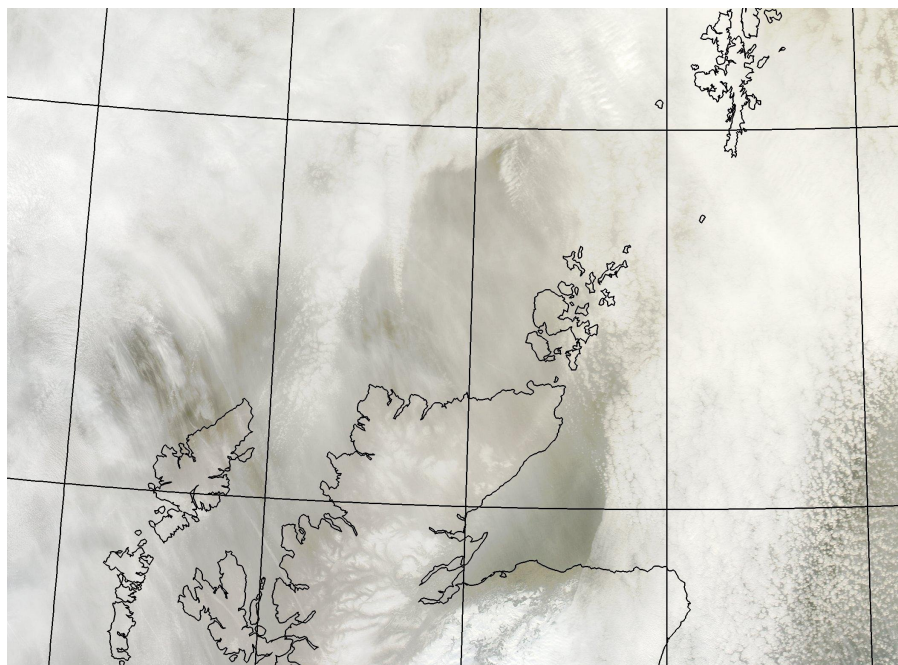



Figure 1. A composite MODIS image of the semi-transparent cirrus case that occurred on 25 January 2010 located over Northern Scotland. The image is from the NERC Satellite Receiving Station, Dundee University, Scotland (<http://www.sat.dundee.ac.uk/>).

Scattering phase function of cirrus and the atmospheric state

A. J. Baran et al.

Title Page

Abstract

Introduction

Conclusions

References

Tables

Figures



Back

Close

Full Screen / Esc

Printer-friendly Version

Interactive Discussion



Scattering phase function of cirrus and the atmospheric state

A. J. Baran et al.

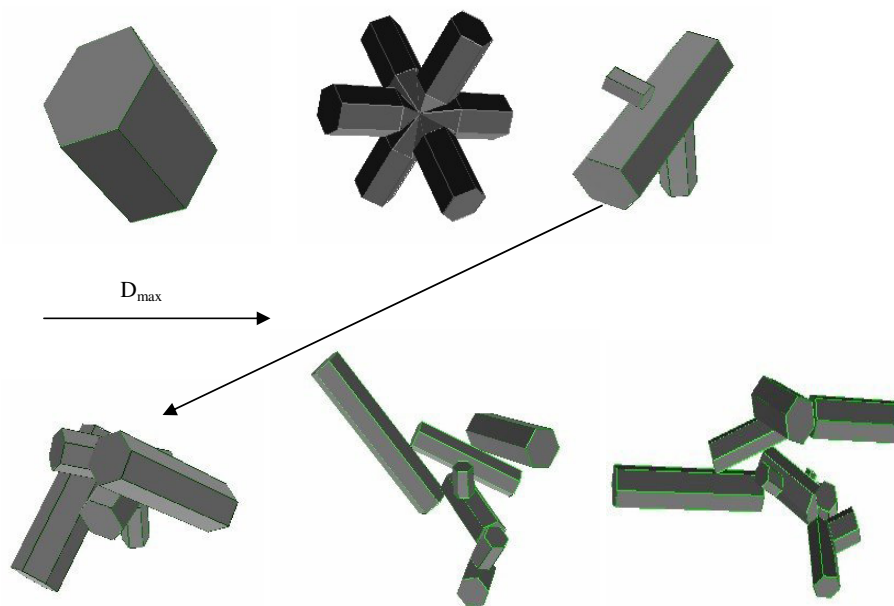


Figure 2. The ensemble model of cirrus ice crystals as a function of ice crystal maximum dimension (D_{max}). The first element of the model is the hexagonal ice column of aspect ratio unity (first panel), six-branched bullet-rosette (second panel), the three-monomer hexagonal ice aggregate (third panel), five-monomer ice aggregate (fourth panel), eight-monomer ice aggregate (fifth panel) and the ten-monomer ice aggregate (sixth panel).

[Title Page](#)[Abstract](#)[Introduction](#)[Conclusions](#)[References](#)[Tables](#)[Figures](#)[◀](#)[▶](#)[◀](#)[▶](#)[Back](#)[Close](#)[Full Screen / Esc](#)[Printer-friendly Version](#)[Interactive Discussion](#)

Scattering phase function of cirrus and the atmospheric state

A. J. Baran et al.

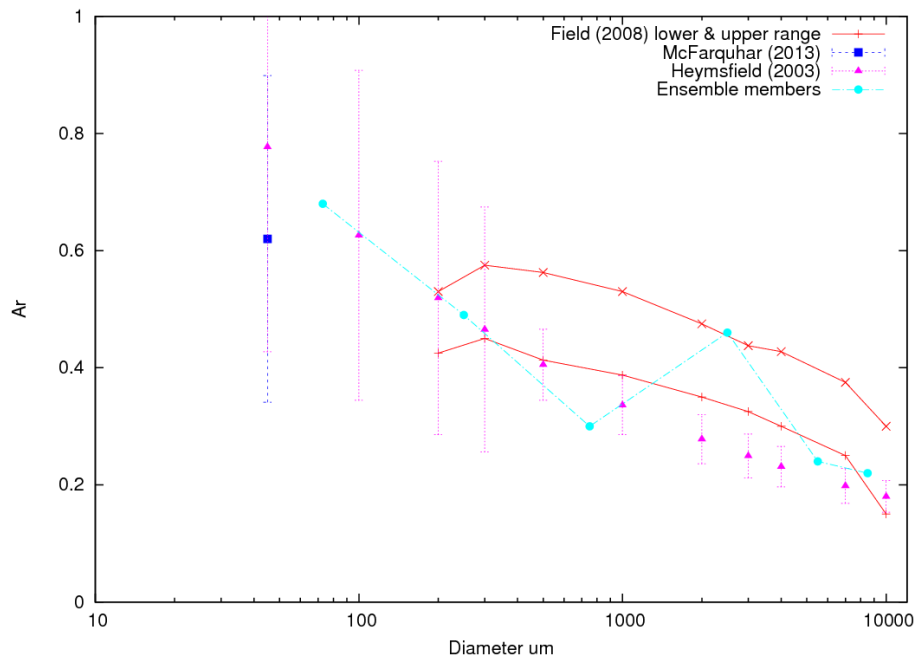


Figure 3. The ensemble model area ratio, A_r , as a function of ice crystal diameter or D_{max} . The key is shown in the upper right-hand side of the figure. The members of the ensemble model are represented by the filled cyan circles. The in situ observations are from Field et al. (2008) represented by the red lines, where the plus and cross signs represent the lower and upper range of those observations and the ranges have an uncertainty of $\pm 30\%$. The blue error bar represents the mean and range of observations taken from McFarquhar et al. (2013) and the purple error bars represent the uncertainty in the observations taken from Heymsfield and Miloshevich (2003).

Scattering phase function of cirrus and the atmospheric state

A. J. Baran et al.

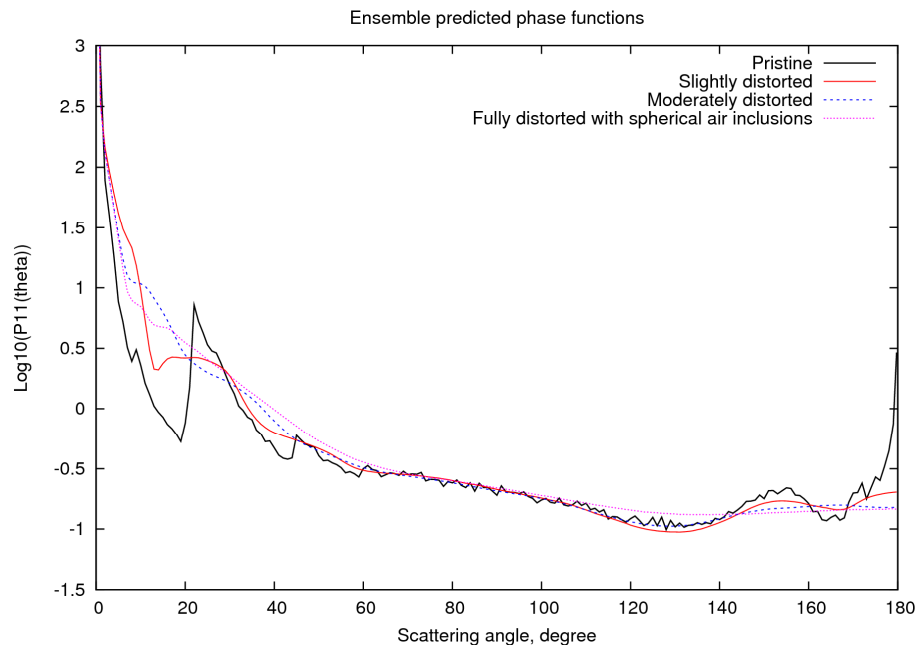


Figure 4. The decadal logarithm of the ensemble model normalised scattering phase function as a function of scattering angle assuming a variety of randomizations. The pristine case (distortion = 0) is represented by the fully line, the slightly distorted case (distortion = 0.15) is represented by the red line. The moderately distorted case (distortion = 0.25) is represented by the dashed blue line and the fully distorted (distortion = 0.40) with spherical air bubble inclusions is represented by the dotted purple line.

[Title Page](#)[Abstract](#)[Introduction](#)[Conclusions](#)[References](#)[Tables](#)[Figures](#)[◀](#)[▶](#)[◀](#)[▶](#)[Back](#)[Close](#)[Full Screen / Esc](#)[Printer-friendly Version](#)[Interactive Discussion](#)

Scattering phase function of cirrus and the atmospheric state

A. J. Baran et al.

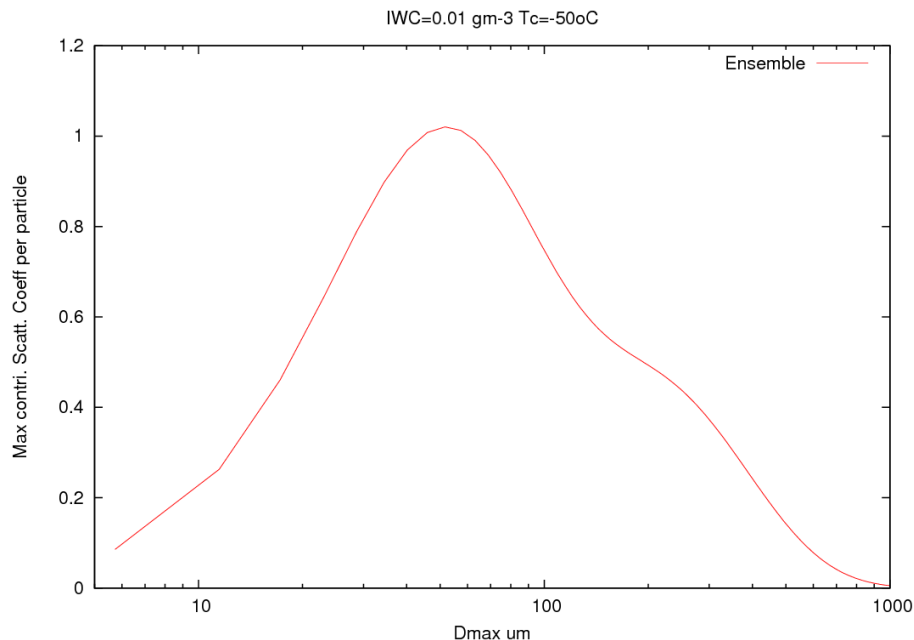


Figure 5. The maximum contribution to the scattering cross section per particle (m^{-2}) as a function of ice crystal maximum dimension D_{max} . The PSD was generated assuming IWC and in-cloud temperature values of 0.01 g m^{-3} and -50°C , respectively.

[Title Page](#)[Abstract](#)[Introduction](#)[Conclusions](#)[References](#)[Tables](#)[Figures](#)[Back](#)[Close](#)[Full Screen / Esc](#)[Printer-friendly Version](#)[Interactive Discussion](#)

Scattering phase
function of cirrus and
the atmospheric state

A. J. Baran et al.

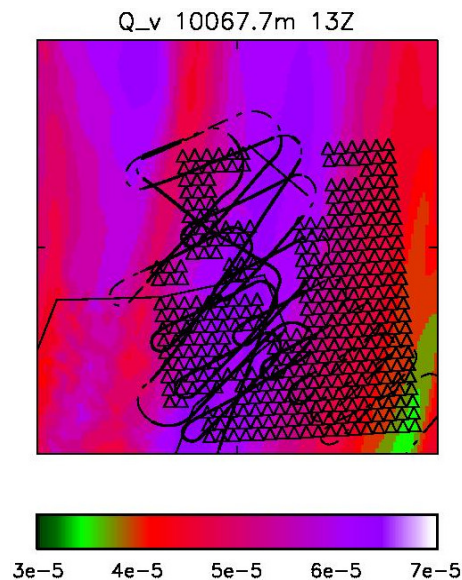


Figure 6. The UKV model field of the water vapour mixing ratio (Q_v) on 25 January 2010 at 13:00 UTC. The units of Q_v are Kg Kg^{-1} . The PARASOL pixels are represented by the triangles and the aircraft track is represented by the full line.

[Title Page](#)[Abstract](#)[Introduction](#)[Conclusions](#)[References](#)[Tables](#)[Figures](#)[Back](#)[Close](#)[Full Screen / Esc](#)[Printer-friendly Version](#)[Interactive Discussion](#)

Scattering phase function of cirrus and the atmospheric state

A. J. Baran et al.

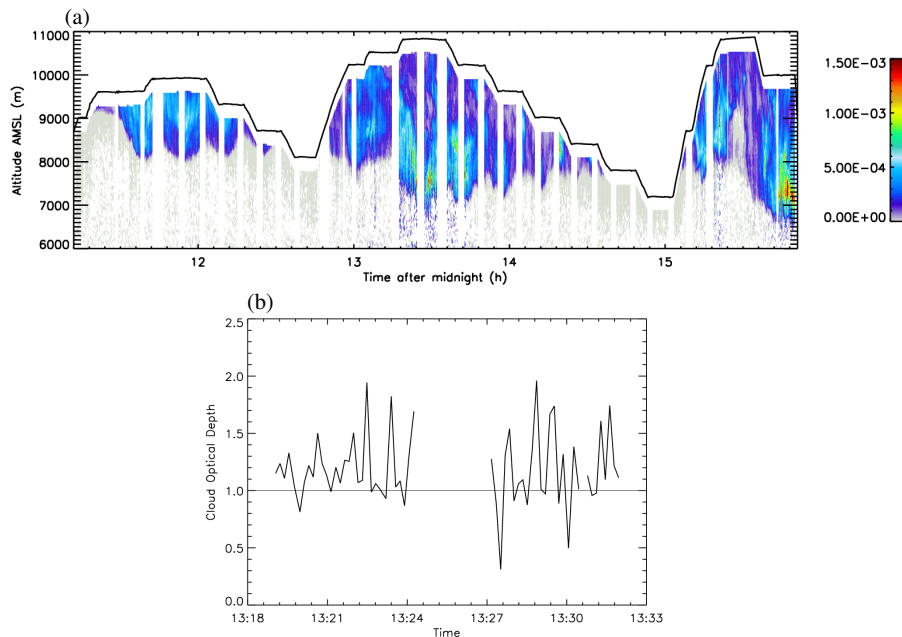


Figure 7. (a) The lidar derived cloud volume extinction coefficient as a function of altitude (m) and time in units of hours after midnight (UTC). The colour bar on the right-hand side of the figure indicates values of the cloud volume extinction coefficient in units of m^{-1} and the full line represents the aircraft altitude. (b) The lidar derived cloud optical depth as a function of time in units of h:min (UTC) and the full line shown in the figure indicates an optical depth value of unity.

Scattering phase function of cirrus and the atmospheric state

A. J. Baran et al.

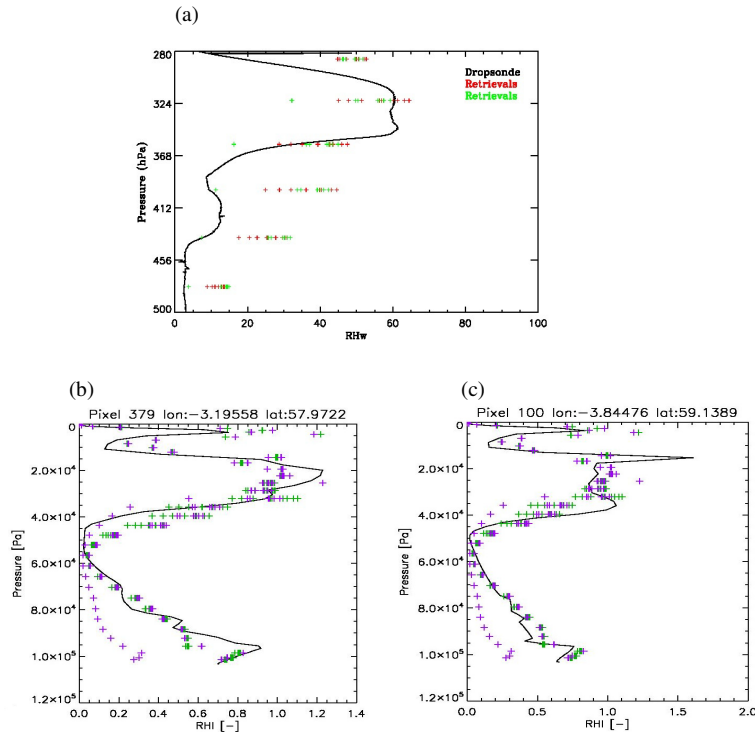


Figure 8. (a) A comparison between the retrieved percentage of RH_w (plus signs) and dropsonde measurements (full line) as a function of altitude in units of hPa. (b) The UKV model and the retrieved vertical profile of RH_v as a function of altitude in units of Pascals (Pa) for the location 57.97° N and 3.196° E and (c) same as (b) but for the location 59.14° N and 3.85° E. In (b) and (c) the UKV model is represented by the full line and retrievals by the purple and green crosses.

Title Page

Abstract

Introduction

Conclusions

References

Tables

Figures

◀

▶

◀

▶

Back

Close

Full Screen / Esc

Printer-friendly Version

Interactive Discussion



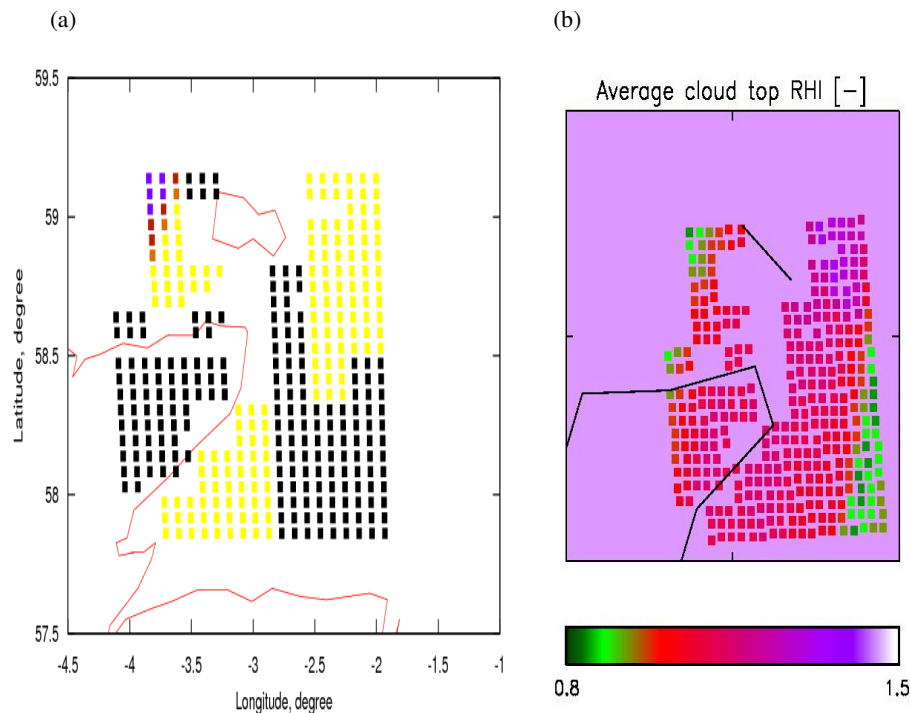


Figure 9. The estimated ice crystal randomization as a function of latitude and longitude. **(a)** The PARASOL estimated ice crystal randomization where the black squares represent the null retrievals. The yellow squares represent the most randomized phase functions (distortion = 0.4 plus spherical air bubble inclusions). The purple squares represent pristine phase functions (distortion = 0), the dark and light brown squares represent the slightly distorted (distortion = 0.15) and moderately distorted (distortion = 0.25) ice crystals, respectively. **(b)** The UKV model predicted RH_i field at cloud-top as a function of latitude and longitude. The model RH_i field has been averaged over the same area as the PARASOL pixels.

Scattering phase function of cirrus and the atmospheric state

A. J. Baran et al.

Title Page	
Abstract	Introduction
Conclusions	References
Tables	Figures
◀	▶
◀	▶
Back	Close
Full Screen / Esc	
Printer-friendly Version	
Interactive Discussion	



Scattering phase function of cirrus and the atmospheric state

A. J. Baran et al.

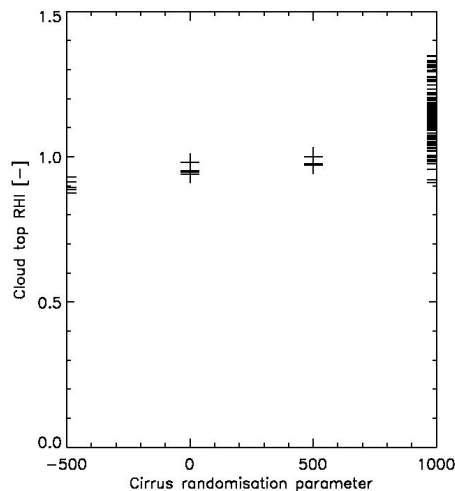


Figure 10. The model predicted RH_i field at cloud-top as a function of estimated ice crystal randomization. On the x-axis the values of -500 , 0 , 500 and 1000 represent ice crystals which are modelled as pristine (distortion = 0), slightly distorted (distortion = 0.15), moderately distorted (distortion = 0.25), and fully distorted (distortion = 0.4 with spherical air inclusions), respectively.

[Title Page](#)[Abstract](#)[Introduction](#)[Conclusions](#)[References](#)[Tables](#)[Figures](#)[◀](#)[▶](#)[◀](#)[▶](#)[Back](#)[Close](#)[Full Screen / Esc](#)[Printer-friendly Version](#)[Interactive Discussion](#)

Scattering phase function of cirrus and the atmospheric state

A. J. Baran et al.

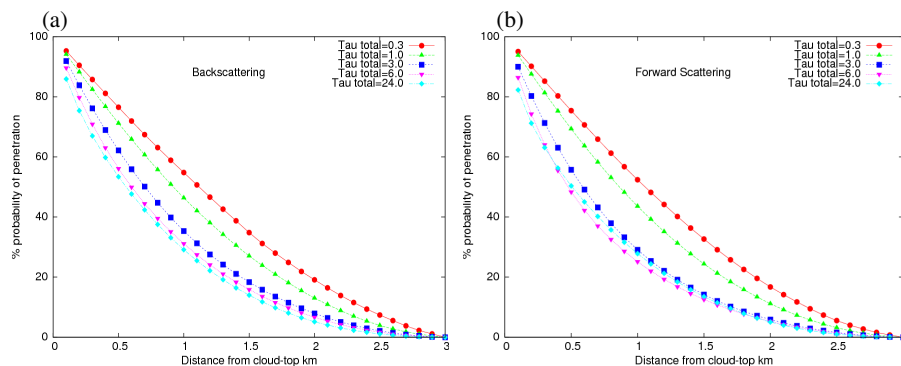


Figure 11. The percent (%) probability of the penetration depth of solar radiation at $0.865 \mu\text{m}$ as a function of distance from the cloud top (km), and cloud optical depth for **(a)** backscattered and **(b)** forward scattered solar radiation in the principal plane, respectively. The key in **(a)** and **(b)** is shown in the upper right-hand side of the figure. The assumed optical depths are 0.3 represented by the red line with filled circles, 1.0 represented by dashed green line with filled triangles, 3.0 represented by dashed blue line with filled squares, 6.0 represented by dotted purple line with inverted filled triangles and 24 represented by dot-dashed light blue line with filled diamonds, respectively.

Scattering phase function of cirrus and the atmospheric state

A. J. Baran et al.

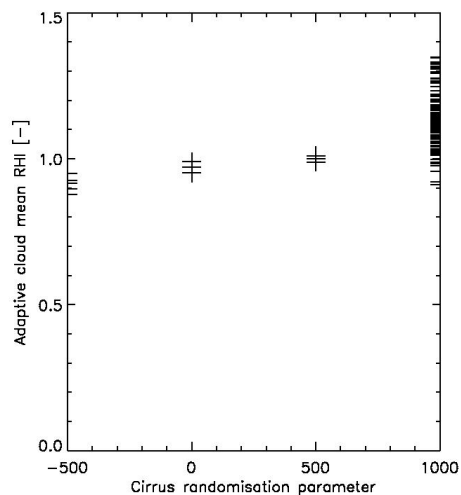


Figure 12. Same as Fig. 10 but for the weighted averaged (adaptive) UKV model RH_i field plotted against the estimated ice crystal randomization.

[Title Page](#)[Abstract](#)[Introduction](#)[Conclusions](#)[References](#)[Tables](#)[Figures](#)[Back](#)[Close](#)[Full Screen / Esc](#)[Printer-friendly Version](#)[Interactive Discussion](#)